

Pseudolite/Ultra-low-cost IMU Integrated Robust Indoor Navigation System Through Real-time Cycle Slip Detection and Compensation

Moon Ki Kim¹, O-Jong Kim¹, Youn Sil Kim², Sang Hoon Jeon¹, Hee Kwon No¹, Beom Ju Shin¹, Jung Beom Kim¹, Changdon Kee^{1†}

¹Mechanical and Aerospace Engineering and the Institute of Advanced Aerospace Technology, Seoul National University, Seoul 151-744, Korea

²SBAS Technology Development Team, Korea Aerospace Research Institute, Daejeon 305-806, Korea

ABSTRACT

In recent years, research has been actively conducted on the navigation in an indoor environment where Global Navigation Satellite System signals are unavailable. Among them, a study performed indoor navigation by integrating pseudolite carrier and Inertial Measurement Unit (IMU) sensor. However, in this case, there was no solution for the cycle slip occurring in the carrier. In another study, cycle slip detection and compensation were performed by integrating Global Positioning System (GPS) and IMU in an outdoor environment. However, in an indoor environment, cycle slip occurs more easily and frequently, and thus the occurrence of half cycle slip also increases. Accordingly, cycle slip detection based on 1 cycle unit has limitations. Therefore, in the present study, the aforementioned problems were resolved by performing indoor navigation through the integration of pseudolite and ultra-low-cost IMU embedded in a smartphone and by performing half cycle slip detection and compensation based on this. In addition, it was verified through the actual implementation of real-time navigation.

Keywords: real-time indoor navigation, 2D pseudolite/ultra-low-cost IMU integration, half cycle slip detection and compensation, smart phone

1. INTRODUCTION

Position information service using the satellite navigation system has been generalized, and it is currently used by many people around the globe. However, the use of the satellite navigation system is unavailable in an indoor environment where the signals transmitted from Global Navigation Satellite System satellites cannot be received. Similar to the necessity of position information in an outdoor environment, there is also a demand for indoor position information. Accordingly, studies on various methods for performing indoor navigation have been attempted. However, as an indoor environment requires more precise navigation and includes more disturbing

factors compared to an outdoor environment, there are difficulties in the development of a reliable system.

In the present study, indoor navigation using pseudolite carrier was implemented among the various methods. For the navigation using carrier, position solution with a high precision can be obtained, but there is a problem of integer ambiguity (Kee et al. 2003a, Yoon 2003). In an indoor environment, navigation can be started with a known initial position, and thus accurate integer ambiguity can be calculated and eliminated at the initial stage (Yoon 2003); but in the case of cycle slip occurrence where the size of the integer ambiguity changes during navigation, the problem of integer ambiguity needs to be resolved (Lee et al. 2010). In a previous study, this problem was resolved by detecting and compensating the cycle slip based on the integration of outdoor Global Positioning System (GPS) and Inertial Measurement Unit (IMU) (Takasu & Yasuda 2008). However, in an indoor environment, cycle slip occurs more frequently compared to an outdoor environment, due to

Received Jul 26, 2017 Revised Jul 31, 2017 Accepted Aug 02, 2017

†Corresponding Author

E-mail: kee@snu.ac.kr

Tel: +82-2-880-8918 Fax: +82-2-876-6649

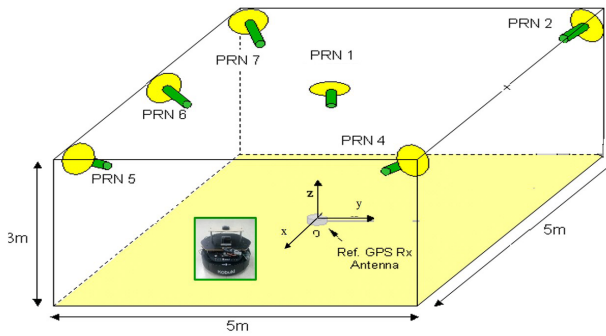


Fig. 1. Pseudolite system indoor.

Table 1. Information about the pseudolite system used.

Number of Pseudolite	Coordinate	Frequency [Hz]
6	Set up indoor	10

signal block, near/far problem, multipath, and others (Kee et al. 2003b, Yoon 2003); and the occurrence of half cycle slip increases accordingly. Therefore, in the present study, for the indoor navigation using pseudolite carrier, half cycle slip was detected and compensated through the integration with ultra-low-cost IMU embedded in a smartphone. In addition, based on this, real-time navigation was implemented using the 'KOBUKI' robot, and the actual operation was examined.

In Chapter 2, the integration of pseudolite and ultra-low-cost IMU based on the Extended Kalman Filter (EKF) is explained; and in Chapter 3, the detection and compensation of half cycle slip are explained. Lastly, in Chapter 4, the implementation of real-time navigation using the 'KOBUKI' robot and a smartphone is presented along with the results.

2. INTEGRATION OF PSEUDOLITE/ULTRA-LOW-COST IMU BASED ON THE EXTENDED KALMAN FILTER

2.1 System Configuration

Fig. 1 and Table 1 show the pseudolite system used in this study.

As for the carrier phase error components, it was assumed that there are no ionospheric error and tropospheric error since it is an indoor environment, and that there are no multipath error and satellite position error as shown in Eq. (1) (Yoon 2003).

$$\phi_u^i = d_u^i - b^i + B_u + N_u^i \lambda + \varepsilon_u^i \quad (1)$$

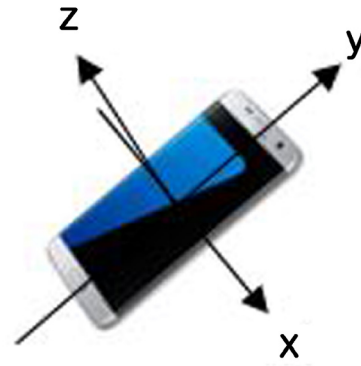


Fig. 2. Body frame of galaxy S7.

The ultra-low-cost IMU sensor used in the present study was the accelerometer and gyroscope embedded in a smartphone (Galaxy S7). Fig. 2 shows the body coordinate system established in the smartphone.

The noise, bias, and scale factor were modeled and utilized. As it was an ultra-low-cost sensor, the performance was not outstanding. In particular, abnormality occurred in the data when the sensor was maintained at a horizontal condition, and the navigation was performed while resolving the abnormality in real time. To transmit the smartphone sensor data, an application was separately manufactured, and the data was transmitted at 100 Hz.

Fig. 3 shows the block diagram of the system. Half cycle slip detection and compensation were added to basic 2D GPS/INS loosely coupled integration. In the case of the velocity measurement, the INS velocity output and CDGPS positioning result were used together.

2.2 Extended Kalman Filter

EKF estimates the position, velocity, attitude, and bias by repeating the process shown in Fig. 4. As it was a 2D assumption, the state included the position, velocity, and attitude in the horizontal direction. In addition, the biases for the accelerometer and gyroscope were estimated and eliminated from the measurement, and this also included only the axes in the horizontal direction, as shown in Eq. (2).

$$State = \begin{bmatrix} y \\ x \\ V_y \\ V_x \\ \psi \\ b_{fx} \\ b_{fy} \\ b_{oz} \end{bmatrix} = \begin{bmatrix} y \text{ axis position} \\ x \text{ axis position} \\ y \text{ axis velocity} \\ x \text{ axis velocity} \\ heading \\ x \text{ axis accelerometer bias} \\ y \text{ axis accelerometer bias} \\ z \text{ axis gyroscope bias} \end{bmatrix} \quad (2)$$

By the coordinate system established in an indoor

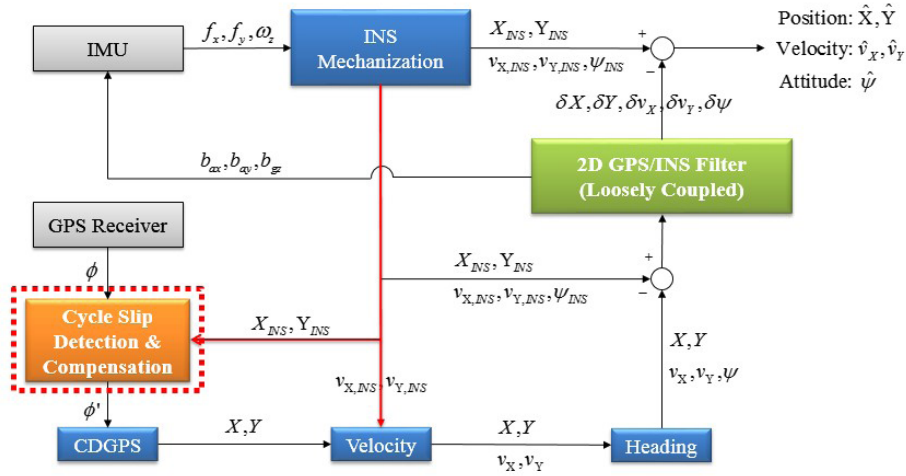


Fig. 3. System block diagram.

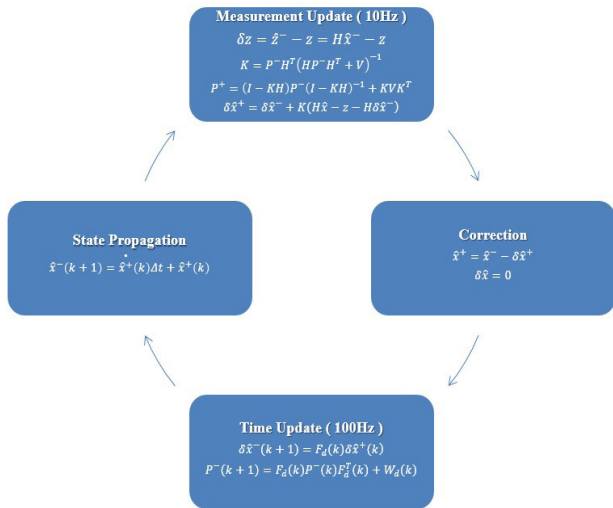


Fig. 4. Extended kalman filter.

environment and the 2D assumption, the nonlinear equation can be organized in a simple form as shown in Eq. (3).

$$\begin{aligned}
 \dot{Y} &= V_y \\
 \dot{X} &= V_x \\
 \begin{bmatrix} \dot{V}_y \\ \dot{V}_x \end{bmatrix} &= \begin{bmatrix} \cos \psi & -\sin \psi \\ \sin \psi & \cos \psi \end{bmatrix} \begin{bmatrix} f_x \\ f_y \end{bmatrix} \\
 \dot{\psi} &= \omega_z \\
 \dot{b}_{fx} &= -\alpha_{fx} b_{fx} \\
 \dot{b}_{fy} &= -\alpha_{fy} b_{fy} \\
 \dot{b}_{\omega z} &= 0
 \end{aligned} \quad (3)$$

After linearization, it is expressed as shown in Eq. (4), and the F and G matrices are expressed by Eq. (5), respectively.

$$\dot{\delta x} = F\delta x + Gw \quad (4)$$

$$F = \begin{bmatrix} 0 & 0 & 1 & 0 & 0 & 0 & 0 & 0 & 0 \\ 0 & 0 & 0 & 1 & 0 & 0 & 0 & 0 & 0 \\ 0 & 0 & 0 & 0 & -f_x \sin \psi & -f_y \cos \psi & -\cos \psi & \sin \psi & 0 \\ 0 & 0 & 0 & 0 & f_x \cos \psi & -f_y \sin \psi & -\sin \psi & -\cos \psi & 0 \\ 0 & 0 & 0 & 0 & 0 & 0 & 0 & 0 & -1 \\ 0 & 0 & 0 & 0 & 0 & 0 & -\alpha_{fx} & 0 & 0 \\ 0 & 0 & 0 & 0 & 0 & 0 & 0 & -\alpha_{fy} & 0 \\ 0 & 0 & 0 & 0 & 0 & 0 & 0 & 0 & 0 \end{bmatrix}$$

$$G = \begin{bmatrix} 0 & 0 & 0 \\ 0 & 0 & 0 \\ \cos \psi & -\sin \psi & 0 \\ \sin \psi & \cos \psi & 0 \\ 0 & 0 & 1 \\ 0 & 0 & 0 \\ 0 & 0 & 0 \\ 0 & 0 & 0 \end{bmatrix} \quad (5)$$

2.3 Sensor Bias Modeling and Data Abnormality Resolution

The bias of the Galaxy S7 accelerometer is a time varying bias, which changes with time. In addition, the gravitational acceleration component that is measured depending on the attitude, as well as the bias of the sensor, exists as the error, as shown in Fig. 5. In the case of 3D, the gravitational acceleration component depending on the attitude change can be the measurement for attitude. However, 2D is assumed in the present study, and thus, all the remaining measurements other than the acceleration measured by actual movement become the error. For example, when there is no actual movement, error can occur if the calculation outputs a result indicating that the position is

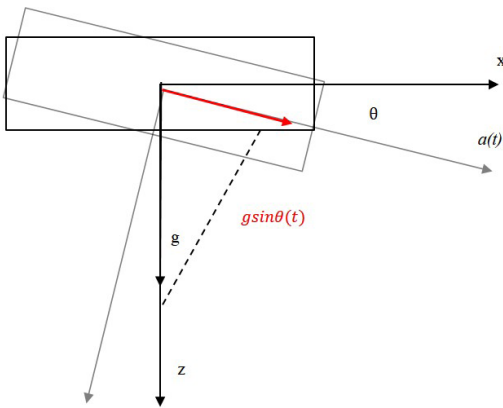


Fig. 5. The gravitational acceleration measured on the horizontal axis according to the attitude.

moving, due to the gravitational acceleration component by attitude. The modeling was performed by including the error due to the gravitational acceleration component in the bias, as shown in Eq. (6).

$$\dot{b} = -ab \tag{6}$$

The gyroscope has a constant bias, and thus it was modeled as shown in Eq. (7).

$$\dot{b} = 0 \tag{7}$$

The data abnormality occurring in the accelerometer is not problematic as the measurement. It is because the abnormality occurs centering on the actual acceleration value to be measured, at a level that is smaller than the noise level. However, the small level can induce a problem for EKF. To eliminate the bias of the accelerometer, bias needs to be estimated. As for the part with abnormality occurrence, the bias cannot be properly estimated because the noise level is too small. When the incorrectly estimated bias is subtracted from the data, the bias error remains by the incorrectly estimated amount, where the error has a larger size and more variation than the existing bias. Thus, before using acceleration data, the data needs to be processed whenever this problem occurs. First, once a value near $\pm 0.045491 \text{ m/s}^2$, which is the acceleration measurement value for abnormality occurrence, is obtained, it is detected as abnormality data. Before use, the detected abnormality data is modified to have an accelerometer normal noise level (0.011 m/s^2) with a mean of $\pm 0.045491 \text{ m/s}^2$.

The abnormality occurring in the gyroscope is the occurrence of a very large data value when the sensor is maintained at a horizontal condition. When this data is used as it stands, a large error would occur, and thus it needs to

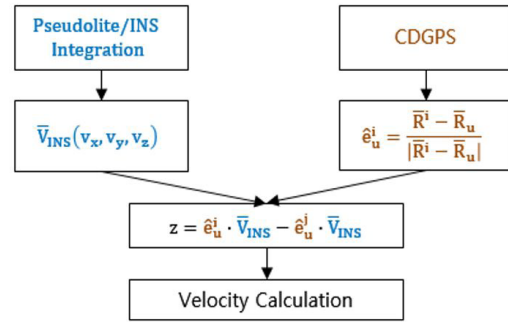


Fig. 6. Calculation of velocity measurement using the velocity result of integrated navigation and position result of CDGPS.

be resolved before use. In this case, the very large data value can be detected and eliminated.

As the present study is based on 2D assumption, only the Z-axis data of the gyroscope is necessary, but the detection of abnormality is impossible using only the Z-axis data. It is because the abnormality and the measurement for rotation cannot be separately detected since the measurement for rotation, which is necessary for our purposes, is recorded in the Z-axis data. However, the abnormality occurs in the X, Y, and Z axes at the same time, and this characteristic can be used to resolve the problem. The detection is performed based on the X-axis or Y-axis; and when abnormality is detected, the Z-axis data of the corresponding epoch is replaced with the Z-axis data of the previous epoch.

2.4 Velocity and Heading Measurement

The velocity measurement can be obtained using Doppler measurement. However, Doppler measurement has relatively larger noise compared to the low velocity of the 'KOBUKI' robot, and thus the velocity is not clearly observed due to the noise. Accordingly, to obtain velocity data with a small noise level, the velocity was calculated using the velocity estimation result of the pseudolite/IMU integrated navigation and the line-of-sight vector calculated from the CDGPS positioning result as shown in Fig. 6, instead of Doppler measurement. The detailed equation is expressed by Eq. (8).

$$\begin{aligned} z &= \Delta \nabla(\dot{d}) \\ &= \Delta \nabla(\dot{D}_u^i \cdot \hat{e}_u^i + D_u^i \dot{e}_u^i \cdot \hat{e}_u^i) \\ &= \Delta \nabla(\dot{D}_u^i \cdot \hat{e}_u^i) \quad (\because e_u^i \cdot \dot{e}_u^i = \frac{1}{2} \frac{d}{dt} (e_u^i \cdot e_u^i) = 0) \\ &= \Delta \nabla((\dot{\hat{R}}^i - \dot{\hat{R}}_u) \cdot \hat{e}_u^i) \\ &= \Delta \nabla(-\dot{\hat{R}}_u \cdot \hat{e}_u^i) \quad (\because \dot{\hat{R}}^i = 0) \\ &= \hat{e}_u^i \cdot \bar{V}_{INS} - e_u^j \cdot \bar{V}_{INS} - (e_u^i \cdot \bar{V}_r - e_u^j \cdot \bar{V}_r) \quad (\because \dot{\hat{R}}_u = \bar{V}_{INS}) \\ &= \hat{e}_u^i \cdot \bar{V}_{INS} - e_u^j \cdot \bar{V}_{INS} \end{aligned} \tag{8}$$

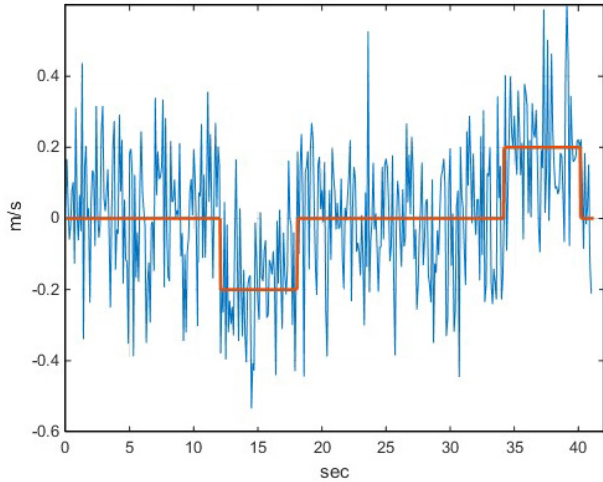


Fig. 7. Velocity measurement using Doppler.

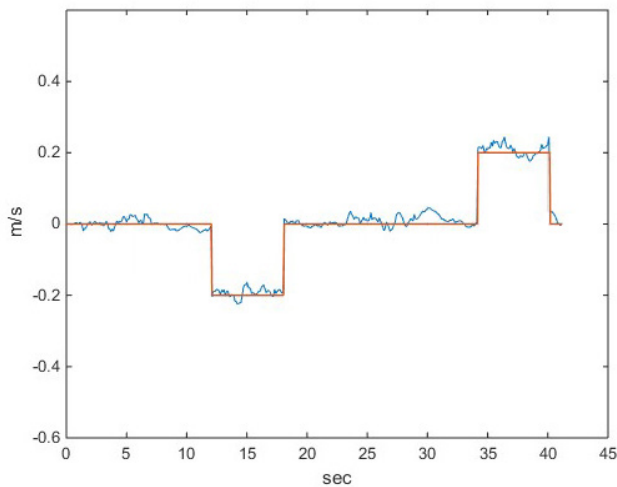


Fig. 8. Velocity measurement using the velocity result of integrated navigation and position result of CDGPS.

As a result, velocity data with a noise level that is much smaller than that of the velocity data using Doppler can be obtained as shown in Figs. 7 and 8.

The velocity measurement obtained using this method has a small noise level, but there is also a problem. As the INS propagation velocity result is used for the velocity measurement calculation, it is directly affected by the acceleration data. There is a large measurement error due to the poor performance of the accelerometer, and the gravitational acceleration components measured in the horizontal direction also become the error by the 2D assumption. As these errors are reflected, fluctuating errors are observed in the velocity measurement besides the noise. This problem can be alleviated by making the movement of the 'KOBUKI' robot smooth, along with filter tuning. By reducing the aforementioned errors as much as possible, the positioning error and the cycle slip monitoring value

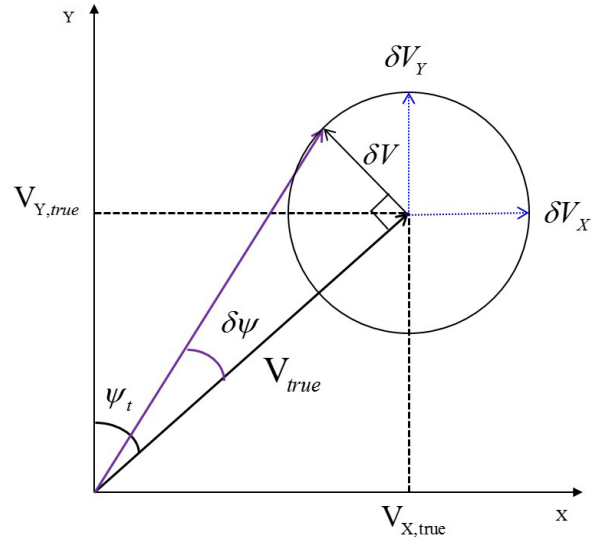


Fig. 9. Relation of velocity error and heading error.

residual error can be decreased.

The heading can be simply calculated using velocity data as shown in Eq. (9).

$$\psi = \tan^{-1} \left(\frac{v_x}{v_y} \right) \quad (9)$$

However, once the heading is calculated at very low velocity, the heading error increases. Accordingly, the lower limit of the velocity for heading calculation needs to be determined, and this was determined based on the following process.

First, a desired heading error level is established. Then, the lower limit of the velocity for heading calculation is determined using the relationship between the velocity error and the heading error as shown in Fig. 9 and Eq. (10) (Kang 2017).

$$\begin{aligned} \delta V &\sim N(0, \sigma_v^2) & \delta \psi &\sim N(0, \sigma_\psi^2) \\ \tan \delta \psi &= \frac{\delta V}{|V_{true}|} \\ \therefore |V_{threshold}| &= \frac{\sigma_v}{\tan \sigma_\psi} \end{aligned} \quad (10)$$

3. HALF CYCLE SLIP DETECTION AND COMPENSATION

3.1 Half Cycle Slip Occurrence for the Indoor Navigation Using Pseudolite Carrier

As for the navigation using carrier, the occurrence of cycle slip is problematic at all times. In particular, for the indoor navigation using pseudolite, cycle slip occurs more

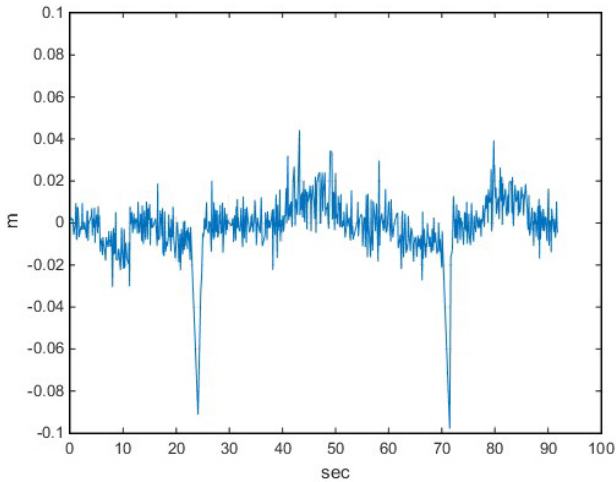


Fig. 10. Occurrence of half cycle slip in ${}^i\nabla^j_r\Delta_u\nabla_t\phi$ graph.

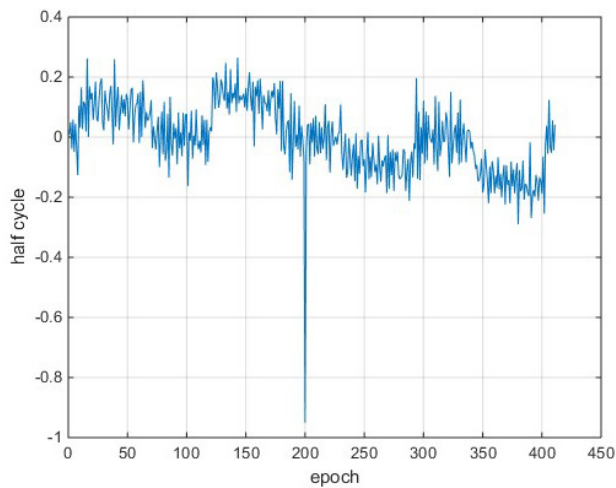


Fig. 11. Existence of distance variation in ${}^i\nabla^j_r\Delta_u\nabla_t\phi$ graph.

easily due to signal block, near/far problem, multipath and others. As the occurrence frequency of cycle slip increases, the occurrence frequency of half cycle slip also increases. The occurrence of half cycle slip can be observed as shown in Fig. 10.

3.2 Cycle Slip Detection Algorithm

The purpose of the method that detects cycle slip through integration with IMU is to enable cycle slip detection in a dynamic condition. It is because the distance change term that exists in the carrier phase measurement in a dynamic condition can be eliminated using the IMU integrated navigation positioning result (Song et al. 2011, Kim et al. 2013, Kim 2016). The detailed explanation is as follows.

Eq. (1) shows the carrier phase error components in an indoor environment. When the double differencing

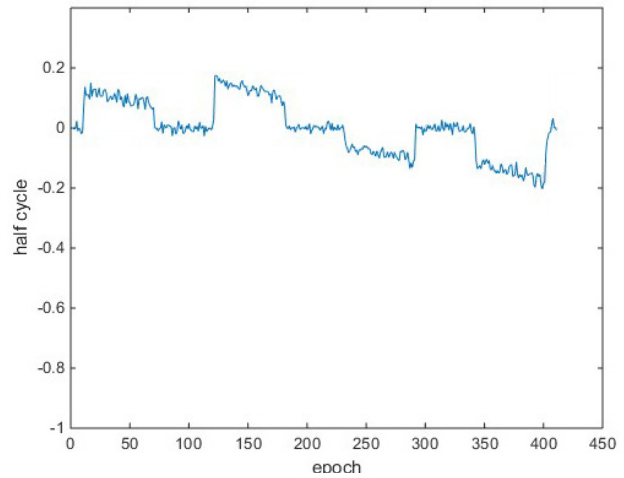


Fig. 12. Distance variation estimated by integrated navigation.

of the carrier phase measured in a dynamic condition is performed and the differencing between epochs is then performed, it can be expressed as shown in Eq. (11). The graph is shown in Fig. 11. As it is a dynamic condition, the d (distance) change term is remained on the right-hand side, and the presence of this term makes it difficult to detect the cycle slip.

$${}^i\nabla^j_r\Delta_u\nabla_t\phi = \nabla\Delta\nabla_t(d + N\lambda + \varepsilon) \quad (11)$$

Thus, the term d needs to be eliminated for the detection of the cycle slip. To eliminate this, the cycle slip detection method based on IMU integration was used in the present study as mentioned earlier. The d change data was made using the positioning result estimated through the integration with IMU, and the equation and graph are shown in Eq. (12) and Fig. 12, respectively.

$$\hat{d}_u^i = |r^i - \hat{r}_u^i|$$

$${}^i\nabla^j_r\Delta_u\nabla_t(\hat{d}_u^i) = {}^i\nabla^j_r\Delta_u\nabla_t(d + \delta d) \quad (12)$$

\hat{r}_u^i : Integrated navigation positioning result
 δd : Integrated navigation distance estimation error

By subtracting the data from the carrier phase where the double differencing and the differencing between epochs have been applied, a monitoring value that can detect the cycle slip can be obtained. The equation is expressed by Eq. (13).

$${}^i\nabla^j_r\Delta_u\nabla_t(d + N\lambda + \varepsilon) - {}^i\nabla^j_r\Delta_u\nabla_t(d + \delta d)$$

$$= {}^i\nabla^j_r\Delta_u\nabla_t(N\lambda + \varepsilon - \delta d) \triangleq \text{Monitoring Value}(m) \quad (13)$$

In the present study, the purpose was to detect the half cycle slip, and thus it was divided by $\lambda/2$ for easy identification, as shown in Eq. (14).

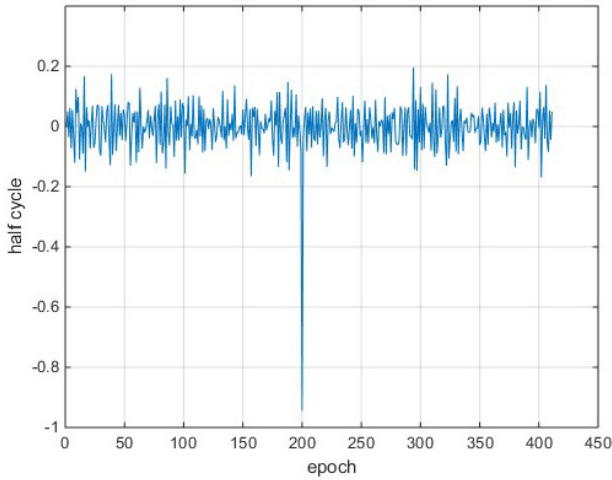


Fig. 13. Distance variation estimated by integrated navigation.

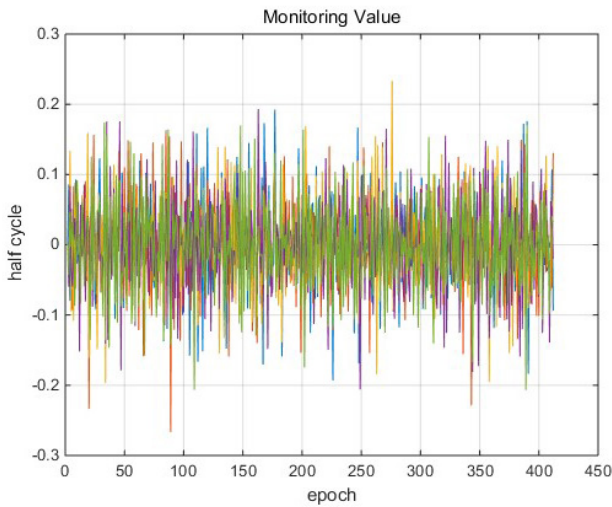


Fig. 14. Real-time Monitoring Value in dynamic situation.

$$\frac{{}^i\nabla^j_r \Delta_u \nabla_t (N\lambda + \varepsilon - \delta d)}{\lambda / 2} \triangleq \text{Monitoring Value (half cycle)} \quad (14)$$

Fig. 13 shows the monitoring value graph where the term d has been eliminated.

3.3 Detection Probability of the Half Cycle Slip

It was examined whether the half cycle slip can be detected probabilistically. Fig. 14 shows the graph that logged the real-time calculation result for the monitoring value in a dynamic condition. As cycle slip did not occur, only the residual error was remained, and it is expressed by Eq. (15).

$$\frac{{}^i\nabla^j_r \Delta_u \nabla_t (\varepsilon - \delta d)}{\lambda / 2} \triangleq \text{Monitoring Value (half cycle)} \quad (15)$$

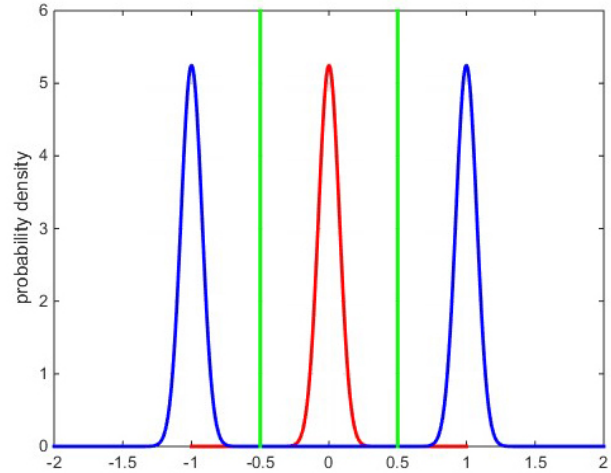


Fig. 15. Probability distribution of monitoring Value residual error and ± 1 half cycle slip.

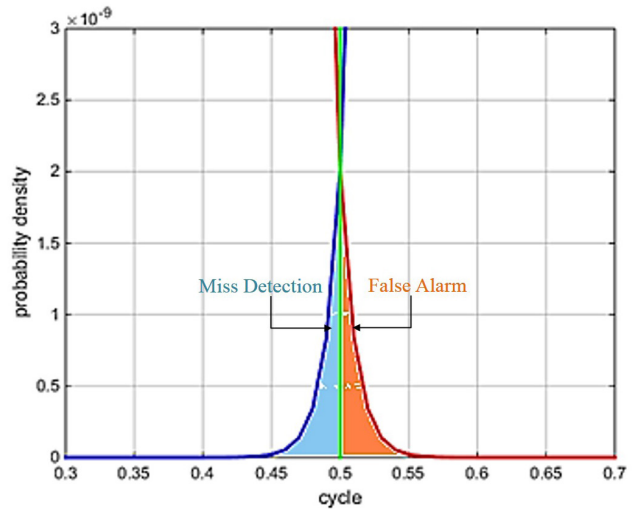


Fig. 16. Magnified graph nearby 0.5 half cycle.

When the 1σ of the data in Fig. 14 was calculated assuming that the residual error has the Gaussian distribution, $1\sigma_{MV}=0.07$ half cycle. Based on this, the probability distribution for the residual error and ± 1 half cycle slip can be drawn as shown in Fig. 15, and the threshold was set to 0.5 half cycle.

To examine the detection probability of half cycle slip, the miss detection and false alarm probabilities were calculated. Fig. 16 shows the magnification of the 0.5 half cycle part in Fig. 15, and the areas marked on the graph represent the probabilities of miss detection and false alarm, respectively.

To increase the detection probability of cycle slip, the probabilities of miss detection and false alarm need to be small. When the values were calculated using the data in Fig. 14, they were very small (both having 10^{-8} level). This

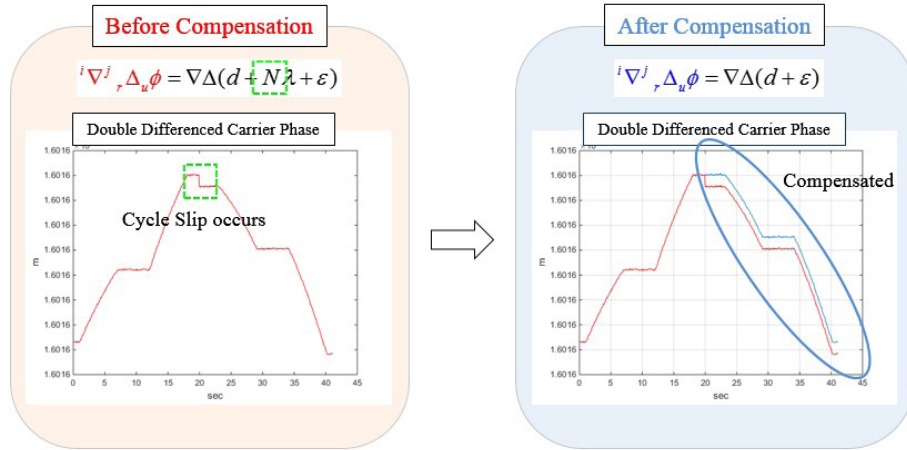


Fig. 17. Before and after cycle slip compensation.

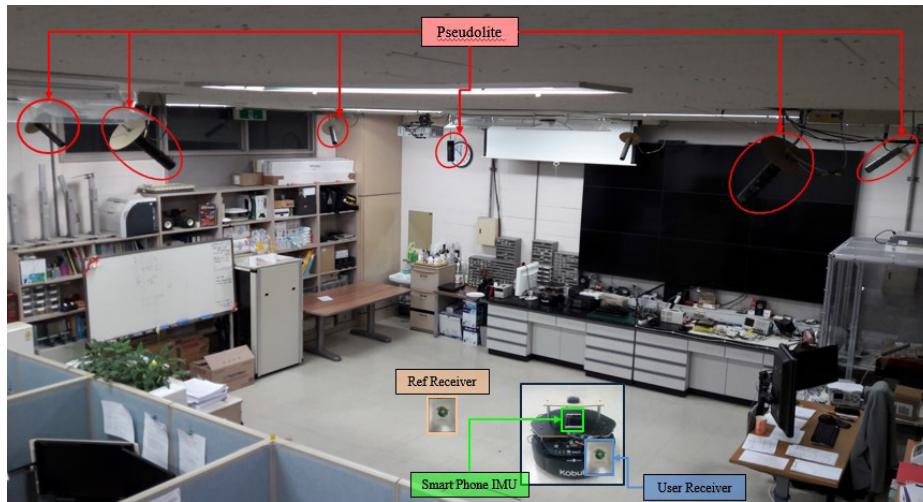


Fig. 18. Indoor experiment environment.

indicates that the half cycle slip can be detected at a very high probability.

3.4 Cycle Slip Compensation Algorithm

Once cycle slip is detected as the monitoring value exceeds the threshold, the change in the cycle is calculated, and it is compensated by that amount. The equation is expressed by Eq. (18).

$$\begin{aligned}
 &{}^i\nabla^j_r\Delta_u\phi_{before} = {}^i\nabla^j_r\Delta_u(d + N\lambda + \varepsilon) \\
 &\text{If Monitoring Value} > \text{threshold} = 0.5 \text{ half cycle} \\
 &N = 0.5 \text{round}(\text{Monitoring Value}) \\
 &{}^i\nabla^j_r\Delta_u\phi_{before} - N\lambda = {}^i\nabla^j_r\Delta_u\phi_{after} \quad (16)
 \end{aligned}$$

The left side of Fig. 17 shows the slip occurring in the double-differenced carrier phase before the cycle slip compensation, and the right side shows the compensated result.

4. REAL-TIME NAVIGATION CONFIGURATION AND RESULTS

4.1 Configuration of the Real-Time Navigation

The experiment was conducted in a space where six pseudolites had been installed on the ceiling, as shown in Fig. 18. The reference station receiving antenna was placed at the origin, and the smartphone, user receiver, and RF modem were installed on the 'KOBUKI' robot. In addition, there was a laptop for performing all the navigation calculations and generating/transmitting the control commands.

The serial communication was organized as shown in Fig. 19. As the reference station receiver was fixed, it transmitted the measurements to the laptop through wired communication at 10 Hz. The user receiver also transmitted the measurements at 10 Hz. At first, the data was transmitted

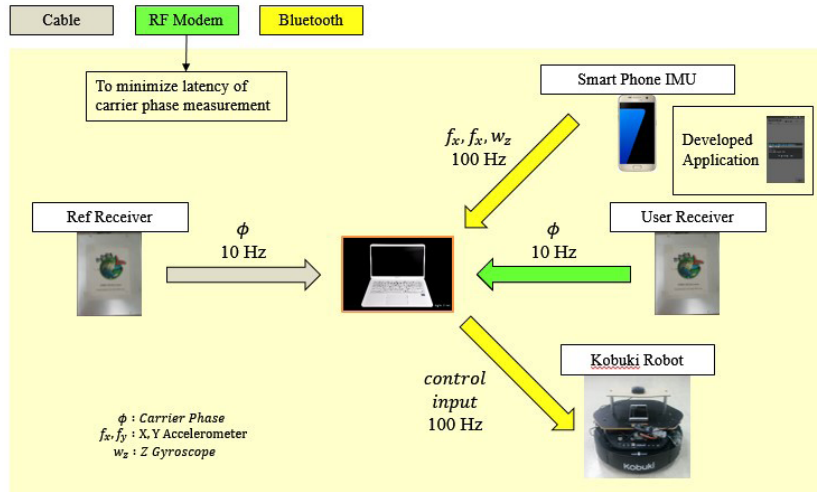


Fig. 19. Configuration of serial communication.

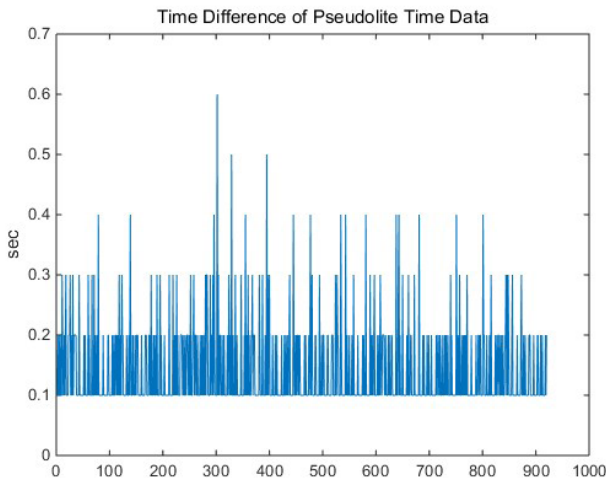


Fig. 20. Time interval transferred by bluetooth.

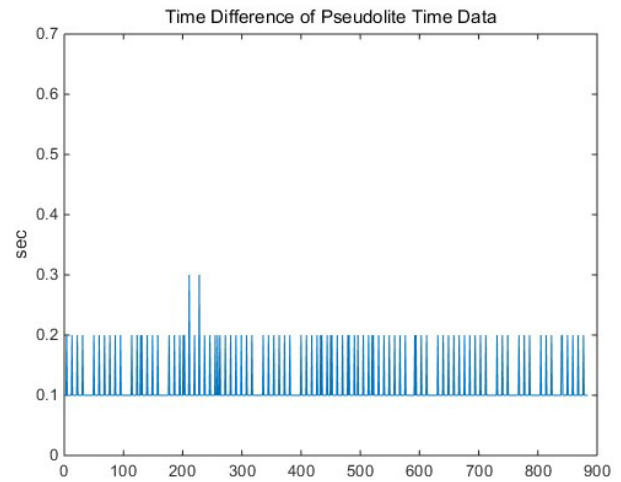


Fig. 22. Time interval transferred by RF modem.

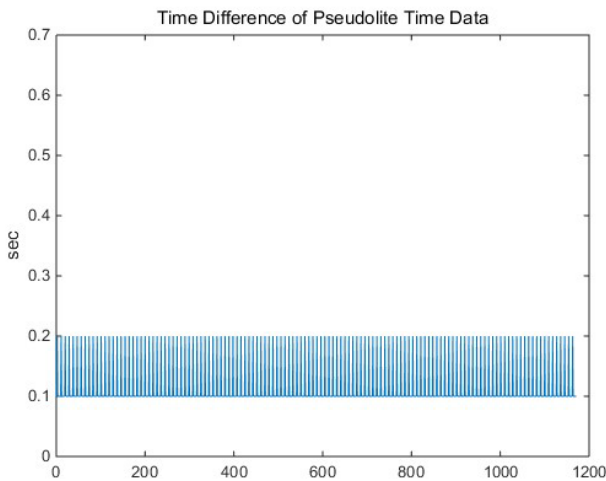


Fig. 21. Time interval transferred by wire.

based on Bluetooth, but it was problematic since Bluetooth had a lot of data loss due to unstable communication (Fig. 20).

When compared to the wired communication (Fig. 21), the problem can be clearly observed.

In the case of the loss of pseudolite data, there is no carrier phase measurement, and thus only INS propagation is performed during the time. In this regard, even when the INS propagation time lengthened slightly, the propagation error increased due to the poor performance of the IMU sensor, which also increased the position error and the cycle slip monitoring value residual error. To resolve this issue, the communication device was changed to RF modem with better communication performance, instead of Bluetooth. As a result, the data loss decreased significantly, as shown in Fig. 22.

The smartphone transmitted the IMU data to the laptop at 100 Hz based on Bluetooth embedded in the smartphone. For the transmission from a smartphone, an Android application is required. As there was no commercial

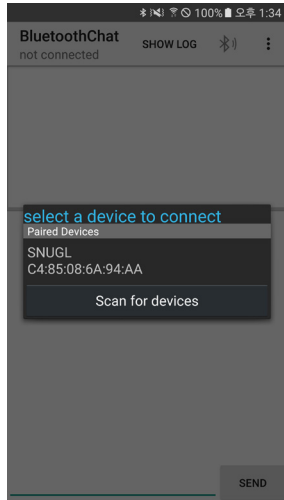


Fig. 23. Smart phone sensor data transmission application developed in this research.

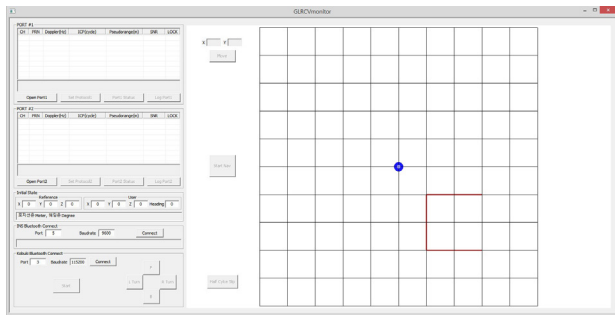


Fig. 24. Real-time navigation program.

application that is capable of the Bluetooth transmission of sensor data, an application was separately manufactured and used as shown in Fig. 23. The control command for the ‘KOBUKI’ robot was transmitted at 100 Hz using Bluetooth embedded in the laptop and the Bluetooth device attached to the ‘KOBUKI’ robot.

Fig. 24 shows the captured screen of the program manufactured for real-time navigation. The manufactured program performs the real-time calculation and positioning result output of the pseudolite/IMU integrated navigation, logging, control command, operation, and imaging. In addition, for the real-time examination of the detection and compensation of the half cycle slip, a generation button was made as shown in Fig. 25 so that half cycle slip can be generated at a desired time. Based on this, a demonstration of the half cycle slip detection and compensation was performed along with real-time images.

4.2 Results

As shown in Fig. 26, the positioning result of the integrated navigation was more precise than that of the

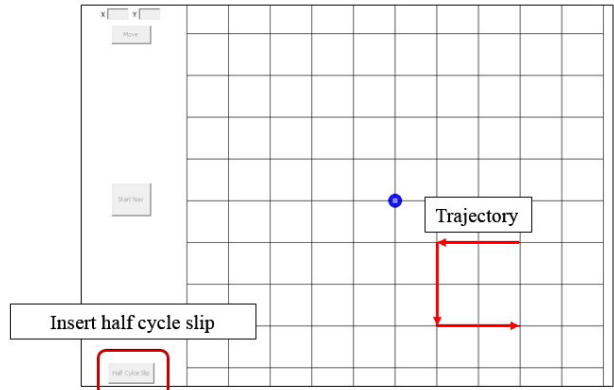


Fig. 25. Occurrence button of half cycle slip.

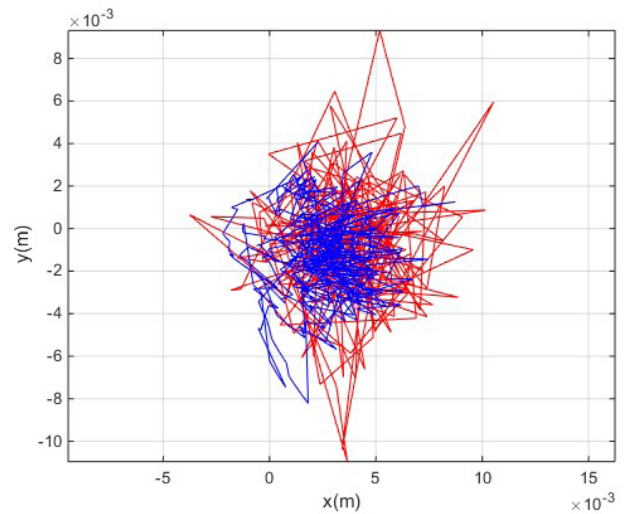


Fig. 26. Position error comparison between pseudolite only and integrated navigation in static situation.

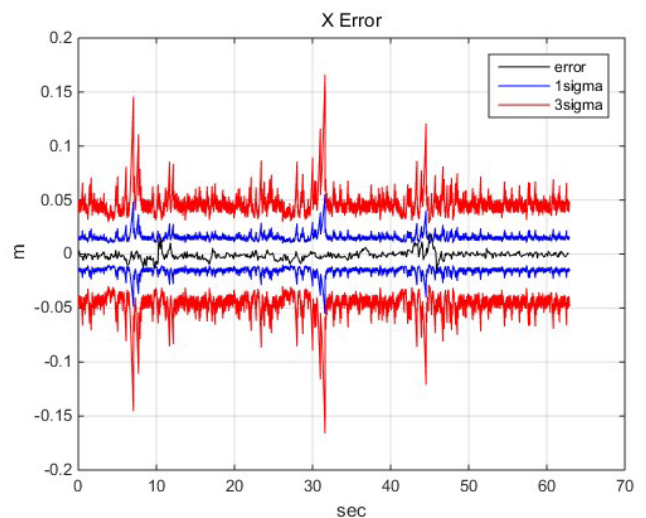


Fig. 27. X axis position error in dynamic situation.

Table 2. Static situation position error. Pseudo-satellite alone vs. integrated navigation results.

1σ [mm]	Pseudolite only	Pseudolite/IMU [mm]
X	2.9	1.9
Y	2.5	1.7

pseudolite-only navigation. Table 2 summarizes the 1σ values for the position error. The integrated navigation showed an approximately 30% improved error level compared to the pseudolite-only navigation. Figs. 27 and 28 show the covariance error bound in a dynamic condition. In the dynamic condition, both the X-axis and the Y-axis were appropriately bounded within 1σ .

In the dynamic condition, half cycle slip was generated for a total of two times using the half cycle slip generator mentioned earlier, and the relevant monitoring value is shown in Fig. 29. Fig. 30 compares the trajectory where error occurred as the half cycle slip was not compensated and the trajectory where error did not occur as the half cycle slip was compensated.

Fig. 31 shows the capture of the real-time image, where

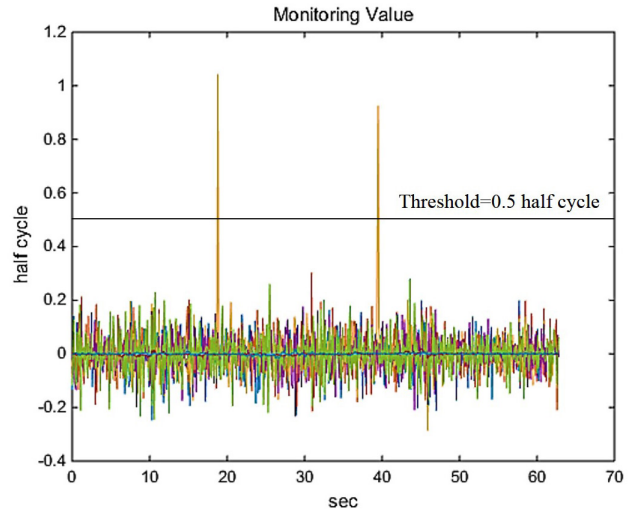


Fig. 29. Monitoring value.

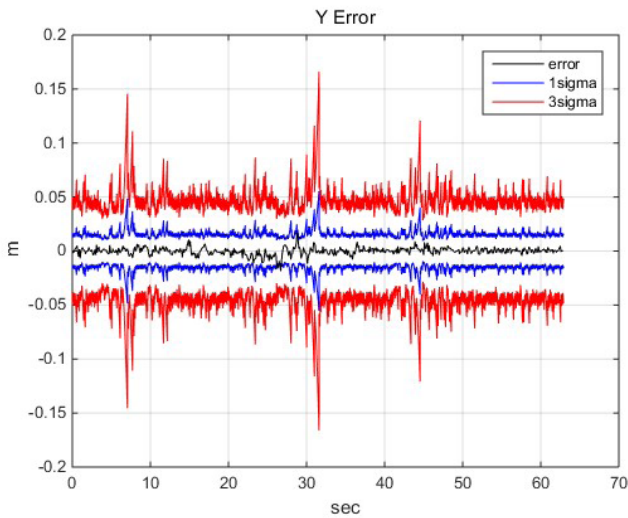


Fig. 28. Y axis position error in dynamic situation.

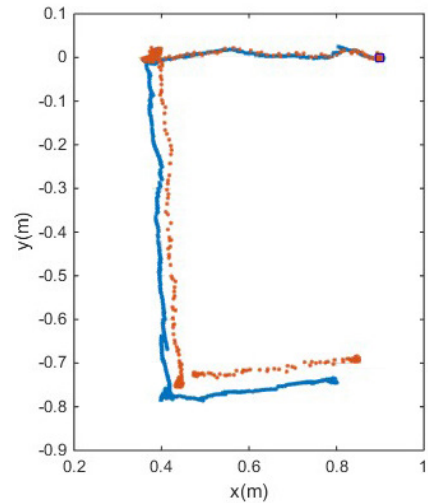


Fig. 30. Half cycle slip compensated trajectory vs. uncompensated trajectory comparison.

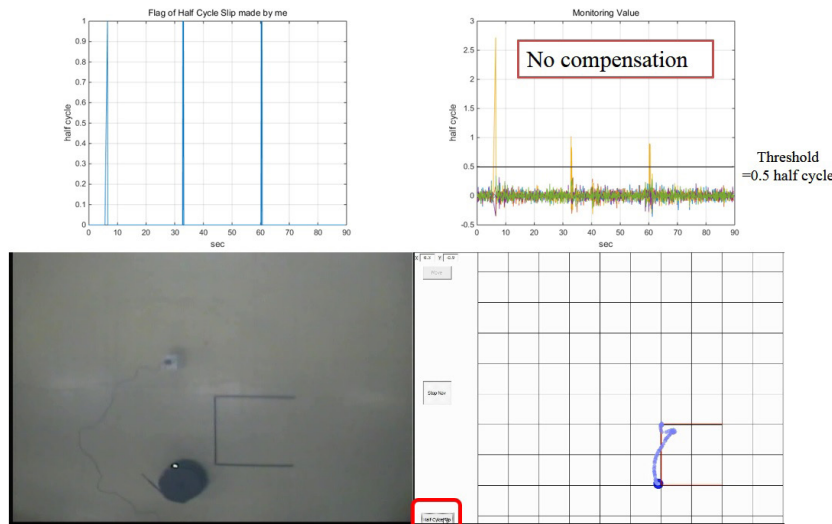


Fig. 31. Real-time video that does not compensate for half-cycle slip.

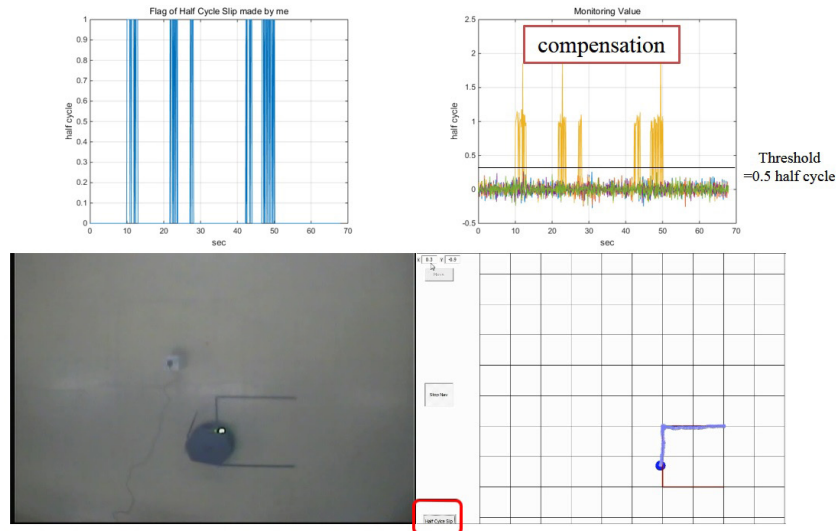


Fig. 32. Real-time video that compensates for half-cycle slip.

position error continuously occurred as half cycle slip was generated and not compensated during the travel. Fig. 32 also shows the capture of the real-time image, where position error did not occur as half cycle slip was continuously generated but compensated during the travel.

5. CONCLUSIONS

This study aimed to resolve the problem of cycle slip occurrence, which had not been resolved in existing indoor navigation research based on pseudolite/IMU integration. In addition, half cycle slip was also detected and compensated by applying the existing cycle slip detection and compensation research based on outdoor GPS/IMU integration to an indoor environment where cycle slip occurs more frequently.

To use the ultra-low-cost IMU sensor embedded in a smartphone for the pseudolite/IMU integration based on EKF, sensor modeling was performed first. When the sensor maintained a horizontal condition, abnormality occurred in the gyroscope and accelerometer. However, this can be resolved, and navigation can be performed in real time without a problem. The filter integration was conducted through simulation, and EKF integration was then completed by performing real-time navigation and by comparing it with the simulation result. It was found that the position accuracy was improved by approximately 30% compared to that of the pseudolite-only navigation.

For the detection of half cycle slip, which is the main topic of the present study, an algorithm was added. To detect half cycle slip, the residual error of the monitoring

value needs to be reduced. For this purpose, the user receiver data was received using RF modem with less data loss, instead of Bluetooth with more data loss. It is because once there is loss of pseudolite data, the propagation error increases since only the INS propagation is performed during the time. Then, to reduce the effect of the accelerometer measurement error, the maneuver of the robot used in the experiment was controlled so that it can move smoothly. It is because abrupt changes in the robot movement induce a large error due to the poor performance of the accelerometer. There are three additional cases that can induce error, but it was assumed that these cases do not happen. After reducing the residual error as mentioned above, the miss detection probability and the false alarm probability were calculated assuming that the level of the residual error is Gaussian. The obtained values were 10^{-8} level, and this indicates that the half cycle slip can be detected at a high probability.

Then, an MFC program that can perform all the algorithms described above in real time was manufactured. Also, an algorithm was added so that the 'KOBUKI' robot at which the smartphone and user receiver had been installed can perform automated travel to a target position. Each device transmitted and received the data based on serial communication through Bluetooth, RF modem, and wired communication. The real-time indoor navigation was organized as described above, and it was found that the half cycle slip can be efficiently detected/compensated and the navigation was appropriately maintained.

ACKNOWLEDGMENTS

This research was supported by a grant (17CTAP-C129724-01) from Technology Advancement Research Program funded by the Ministry of Land, Infrastructure, and Transport of Korean government, contracted through SNU-IAMD at the Seoul National University.

REFERENCES

- Kang, M. 2017, A study on improvement of navigation performance of land vehicle using low cost 2D DGPS/INS/Magnetometer considering gravity, Master's Thesis, Seoul National University, Korea
- Kee, C., Jun, H., & Yun, D. 2003a, Indoor Navigation System using Asynchronous Pseudolites, *The Journal of Navigation*, 56, 443-455. <https://doi.org/10.1017/S0373463303002467>
- Kee, C., Yun, D., & Jun, H. 2003b, Precise calibration method of pseudolite positions in indoor navigation systems, *Computers & Mathematics with Applications*, 46, 1711-1724. [https://doi.org/10.1016/S0898-1221\(03\)90205-7](https://doi.org/10.1016/S0898-1221(03)90205-7)
- Kim, Y. 2016, A study on cycle slip detection of single frequency GNSS receiver using low cost INS, Ph.D. Thesis, Seoul National University, Korea
- Kim, Y., Song, J., Yun, H., Park, B., & Kee, C. 2013, GPS Cycle-slip Detection with Low-cost IMU and Single-frequency Receiver of Land Vehicle, *Proceedings of the ION 2013 Pacific PNT Meeting*, April 23-25, 2013, Honolulu, Hawaii, pp.1032-1039
- Lee, T., Kim, C., Jeon, S., Jeon, S., Kim, G., et al. 2010, Pedestrian Indoor Navigation Algorithm based on the Pseudolite and Low-cost IMU with Magnetometers Including In-Flight Calibration, *Proceedings of the 2010 International Technical Meeting of The Institute of Navigation*, January 25-27, 2010, San Diego, CA, pp. 230-235. <https://www.ion.org/publications/abstract.cfm?articleID=8801>
- Song, J., Park, B., Yun, H., & Kee, C. 2011, Odometer-Aided Real Time Cycle Slip Detection Algorithm for Land Vehicle Users, *Proceedings of the 2011 International Technical Meeting of The Institute of Navigation*, January 24-26, 2011, San Diego, CA, pp.326-335. <https://www.ion.org/publications/abstract.cfm?articleID=9474>
- Takasu, T. & Yasuda, A. 2008, Cycle Slip Detection and Fixing by MEMS-IMU/GPS Integration for Mobile Environment RTK-GPS, *Proceedings of the 21st International Technical Meeting of the Satellite Division of The Institute of Navigation (ION GNSS 2008)*,

Savannah, GA, pp.64-71

Yoon, D. 2003, A Study on GPS pseudolite navigation system, Ph.D. Thesis, Seoul National University, Korea



Moon Ki Kim is a M.S. candidate of GNSS Lab in the School of Mechanical and Aerospace Engineering at Seoul National University. He received B.S. degree in aerospace and mechanical engineering from Korea Aerospace University. His research interests include Pseudolite / IMU integrated indoor navigation and cycle slip detection / compensation.



O-Jong Kim is a Ph.D. candidate in the School of Mechanical and Aerospace Engineering at Seoul National University, South Korea. He received the B.S. degree and Master degree from Seoul National University. His research interests include alternative PNT, cycle ambiguity resolution and cube-satellite.



Youn Sil Kim is a senior researcher in the SBAS technology development team at Korea Aerospace Research Institute. She received a B.S. degree in aerospace engineering at Sejong University and received a M.S and Ph.D. degree in the School of Mechanical and Aerospace Engineering at Seoul National University. And She had been a postdoctoral researcher in the School of Mechanical and Aerospace Engineering at Seoul National University. Her research interests are the inertial navigation, GPS/INS integrated navigation, carrier-phase cycle slip detection, single frequency carrier phase based navigation algorithm.



Sang Hoon Jeon is a contract assistant professor in BK21Plus Transformative Training Program for Creative Mechanical and Aerospace Engineers at Seoul National University. His received the B.S. and Doctoral degree in 2012 from Seoul National University and worked at DMC research center and mobile division of Samsung electronics. His recent research interests include GNSS receiver technology, software defined radio and sensor integration system for indoor navigation.



Hee Kwon No is a postdoctoral researcher in the School of Mechanical and Aerospace Engineering at Seoul National University. He received B.S. and Ph.D. degrees from the same university. His research interests are the cost effective attitude determination, navigation, guidance and automatic control system of the unmanned aerial vehicle.



Beom Ju Shin received his BS and MS degrees in information and communication engineering from Sejong University, Seoul, Rep. of Korea, in 2010 and 2012, respectively. From 2012 to 2014, he worked for the Sensor System Research Center at the Korea Institute of Science and Technology, Seoul, Rep. of Korea. He is currently working toward his PhD at the School of Mechanical and Aerospace Engineering, Seoul National University, Seoul, Rep. of Korea. His current interests include pattern recognition, machine learning, and indoor navigation system.



Jung Beom Kim is a Ph.D. candidate of GNSS Lab. in the School of Mechanical and Aerospace Engineering at Seoul National University. He received the B.S and Master degree from Seoul National University. His recent research interests DGPS, FKP and Improvement of L1 single frequency GPS receiver's positioning accuracy.



Changdon Kee is a Professor in the School of Mechanical and Aerospace Engineering at Seoul National University (SNU), South Korea and supervises SNU GNSS Lab (SNUGL, <http://gnss.snu.ac.kr>). He received B.S. and M.S. degrees from Seoul National University and a Ph.D. degree from Stanford University. He served as a Technical Advisor to the Federal Aviation Administration (FAA) on the Wide Area Augmentation System (WAAS) in 1994. Prof. Kee currently serves as a Technical Advisor for Korea Civil Aviation Safety Authority (KCASA) and Ministry of Public Administration and Security (MOPAS). He also serves as a President of Korean Institute of Navigation. He has more than 20 years of GNSS and flight control research experiences.